A Panoramic Synthetic Aperture Radar

Yijiang Nan, Xiaojing Huang, *Senior Member, IEEE,* and Y. Jay Guo, *Fellow, IEEE*

***Abstract*—This paper develops a new ground-based synthetic aperture radar (GB-SAR) concept based on a combination of linear and rotation GB-SARs, by which a panoramic observed view is provided, thus named as panoramic SAR. Firstly, the system geometry and its imaging process based on the back-projection algorithm (BPA) are presented. The combined movement formulates a two-dimensional synthetic aperture and thus higher imaging resolutions can be obtained. The corresponding resolution analysis and the sampling criteria are discussed accordingly. Then, a novel dynamic piecewise constant (DPC) algorithm is proposed to reduce the complexity significantly, by which a recursive imaging process can be achieved. The imaging implementation and the complexity are also studied respectively. Finally, a prototype of panoramic SAR is built up based on a FMCW radar and a moving platform, and the simulation and experimental results are provided to validate the proposed SAR principle and the DPC algorithm.**

***Index Terms*—ground-based SAR, panoramic SAR, back-projection algorithm, dynamic piecewise constant algorithm, recursive imaging.**

I. Introduction

SYNTHETIC aperture radar as an important remote sensing technique can reconstruct a high-resolution image of the observed targets [1]. It can work day and night under all weather conditions by using its own illumination, and has been widely used in civilian and defense applications [2]–[4]. Conventional SAR systems are always mounted on the airplanes or satellites and illuminate the targets using a pulsed side-looking radar. Such a heavy and high-cost radar system with an inflexible moving trajectory are not available for the frequent visits. To achieve the continuous ground monitoring of a small coverage, the ground-based SAR (GB-SAR) has been proposed in the last decades as a portable and low-cost geotechnical instrument which plays an important role in automotive-terrain imaging [5], [6], deformation monitoring and disaster prevention [7], [8].

Existing GB-SAR systems can be classified into two categories, i.e., linear GB-SAR [9], [10] and rotation GB-SAR [11], [12], in terms of the synthetic aperture trajectory. Conventional linear GB-SARs are normally based on a continuous-wave stepped-frequency radar, and the synthetic aperture is achieved by moving antenna on a rail as shown in Fig. 1a. Due to the side-looking radar, only the targets located at one side can be imaged. Recently, the linear GB-SARs working with a forward-looking radar were well reported [13] and the imaging capabilities have been significantly improved using low-THz (150 GHz) radars [14] with frequency modulated continuous wave (FMCW) signalling. However, the improvement of the angular/azimuth resolution is a great challenge and the angular width of the observation is still limited.

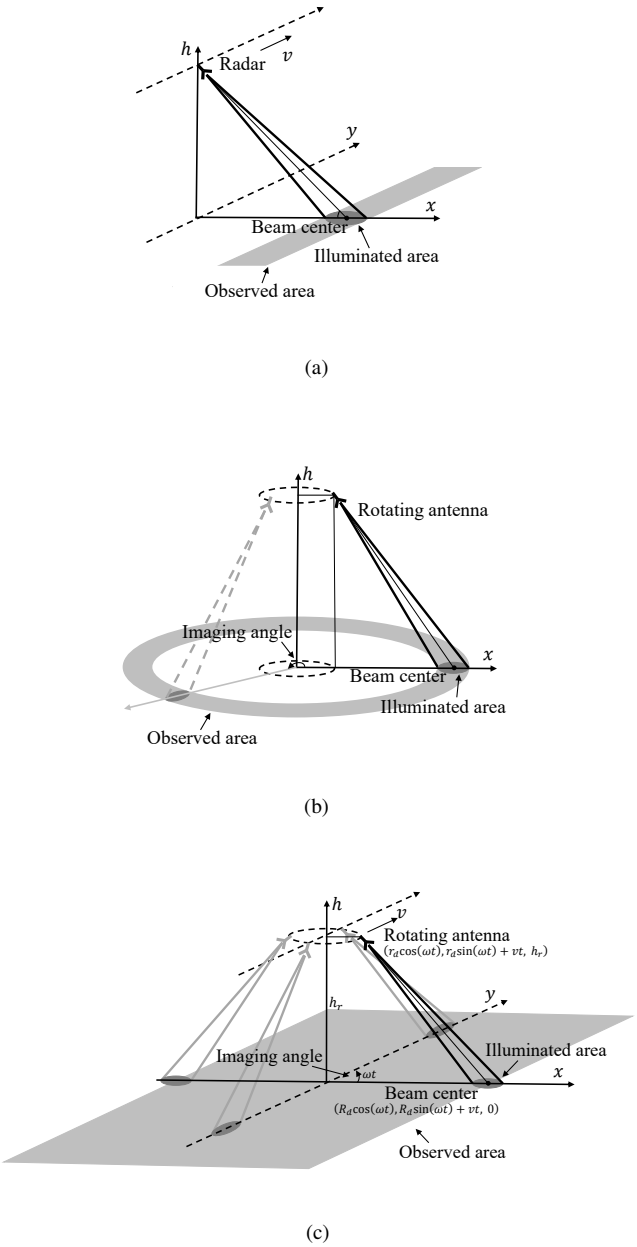

Fig. 1. Geometry of GB-SARs: (a) linear SAR, (b) rotation SAR, and (c) panoramic SAR.

In rotation GB-SAR, the aperture is always synthesized using an antenna mounted on the tips of a helicopter rotor blade as shown in Fig. 1(b). With a fixed beam steering, radar images at 360 degree can be reconstructed. To simplify

This work was supported under the Australian Research Council (ARC) Discovery Project DP 160101693.

Yijiang Nan, Xiaojing Huang and Y. Jay Guo are with the Global Big Data Technologies Center, University of Technology Sydney, NSW, Australia, e-mails: Yijiang.Nan@uts.edu.au, Xiaojing.Huang@uts.edu.au, Jay.Guo@uts.edu.au.

the deployment, a new version of rotation GB-SAR was developed named ArcSAR [15]–[17] using FMCW radar fixed on a rotating arm controlled by a step motor. However, the angular/azimuth resolution is determined by the radius of the rotation and the angular width of the antenna. A relatively short arm leads to a worse resolution than that of the linear one. Additionally, the beamwidth of the antenna in elevation limits the observed area.

To tackle the above-mentioned limitations, this article develops a novel panoramic SAR concept as a combination of linear and rotation SARs. The radar is fixed on a rotating arm and at the same time moves linearly along $y-$direction mounted on a vehicle with a constant speed v as shown in Fig. 1c, by which a larger panoramic view can be provided. The combined movement formulates a two-dimensional (2-D) synthetic aperture larger than that of linear or rotation SARs, and thus higher imaging resolutions can be obtained. In panoramic SAR, the nonorthogonality between the rotating and linear movements leads to two challenges for the imaging process, i.e., the nonlinear spatial sampling and the spatially variant synthetic aperture corresponding to the targets located at different imaging angle shown in Fig. 1c. Therefore, the Fourier-based SAR imaging methods are no longer valid for the panoramic SAR. The back-projection algorithms (BPAs) can deal with this problem in time-domain [18], [19], but the huge computational cost and data storage limit its applications. Some fast BPAs has been proposed based on aperture factorization and recursive partition of the imaging integral [20], [21], but they are not valid due to this nonorthogonality of the panoramic SAR movement.

In this article, we firstly investigate the theory of the panoramic SAR, including system geometry, BPA imaging process, analyses of imaging resolutions and sampling criteria. Then, a novel fast dynamic piecewise compensating (DPC) algorithm is proposed to tackle the spatially variant 2-D synthetic aperture, by which the difference of the slant range surface between two adjacent imaging targets can be compensated dynamically based on the imaging angle and thus a recursive imaging process can be conducted. Finally, the panoramic SAR is prototyped by using a FMCW radar mounted on a moving platform. The experimental and simulation results can validate the panoramic SAR theory and the superior imaging performance and efficiency of the proposed algorithm.

The remainder of this paper is organized as follows. The theory of panoramic SAR and the corresponding DPC algorithm are derived in Section II and III respectively. The prototype of panoramic SAR and the imaging results are shown in Section IV. Section V concludes the whole work.

II. Panoramic SAR Principle

In this section, we present the system geometry of panoramic SAR, derive the corresponding BPA-based imaging process, and analyze the imaging resolutions and sampling criteria.

A. System Geometry

The geometry of panoramic SAR is presented in Fig. 1c with a Cartesian coordinate system. A transceiver antenna is fixed on the tip of a rotating arm with a radius of r_d and an angular speed of ω. The center of the rotation, at $x = 0$ and $h = h_r$, moves linearly along $y-$direction with a speed of v. Assuming that the initial position of the transceiver is $(r_d, 0, h_r)$, the instantaneous slant range with respect to the time t between the transceiver and the imaging target located at the point $(x', y', 0)$ can be expressed as

$$\begin{aligned} &r(t; x', y') \\ &= \left((r_d cos(\omega t) - x')^2 + (r_d sin(\omega t) + vt - y')^2 + h_r^2\right)^{1/2} \end{aligned} \tag{1}$$

which is a 1-D function of t. To reflect the rotating and linear movements respectively, (1) can be represented as a 2-D function with respect to the rotating angle and forward distance of the transceiver position, $\varphi = \omega t$ and $y = vt$. With a fixed side-looking radar, the beam footprint has the same trajectory but with a larger radius as that of the antenna as shown in Fig. 1c. To catch the maximum reflected power, the imaging targets at the trajectory of the beam center are reconstructed. Therefore the imaging target locations can be transformed into $(R_d cos(\varphi'), R_d sin(\varphi') + y')$ and (1) can be derived as

$$\begin{aligned} &r(\varphi, y; \varphi', y') \\ &= \Big((r_d cos(\varphi) - R_d cos(\varphi'))^2 \\ &+ (r_d sin(\varphi) - R_d sin(\varphi') + y - y')^2 + h_r^2\Big)^{1/2} \end{aligned} \tag{2}$$

where R_d is the radius of the rotating beam center, φ' and y' are values of the imaging target location with respect to φ and y respectively.

To achieve a 2-D spatial sampling, a frequency modulated continuous wave (FMCW) signal is emitted periodically by the transceiver. Assuming that the stop-and-go approximation is valid and the propagation attenuation is neglected, after demodulation, the backscattered echoes can be expressed as

$$\begin{aligned} E_r(\tau; \varphi, y) = &\int\int \sigma(\varphi', y') exp(-j2\pi(f_c + K_r\tau) \\ &\cdot \frac{2r(\varphi, y; \varphi', y')}{c} + j\pi K_r(\frac{2r(\varphi, y; \varphi', y')}{c})^2) d\varphi' dy' \end{aligned} \tag{3}$$

where τ is the fast time, $\sigma(\varphi', y')$ is the radar cross section (RCS) of the target at $(R_d cos(\varphi'), R_d sin(\varphi') + y')$, K_r is the chirp rate, and c is the speed of light. After removing the residual video phase, (3) becomes a function of the spatial wavenumber k, expressed as

$$\begin{aligned} E_r(k; \varphi, y) &= \int\int \sigma(\varphi', y') exp(-j2\pi(f_c + K_r\tau) \\ &\cdot \frac{2r(\varphi, y; \varphi', y')}{c}) d\varphi' dy' \\ &= \int\int \sigma(\varphi', y') exp(-j2kr(\varphi, y; \varphi', y')) d\varphi' dy' \end{aligned} \tag{4}$$

and $k = 2\pi(f_c + K_r\tau)/c$ is the spatial wavenumber.

B. BPA Imaging Process

With the conventional BPA, the range compression is firstly achieved by the inverse FFT (IFFT) operation with respect to the wavenumber k as

$$\begin{aligned} & e_r(\rho';\varphi,y) \\ &= \int E_r(k;\varphi,y)exp(j2k\rho')dk \\ &= \int\int\int \sigma(\varphi',y')exp(-j\frac{4\pi}{\lambda_c}r(\varphi,y;\varphi',y')) \\ &\cdot \int_{-\frac{\pi B}{c}}^{\frac{\pi B}{c}} exp(j2k(\rho'-r(\varphi,y;\varphi',y')))dkd\varphi'dy' \\ &= \int\int \sigma(\varphi',y')exp(-j\frac{4\pi}{\lambda_c}r(\varphi,y;\varphi',y')) \\ &\cdot \frac{2\pi B}{c}sinc(\frac{2\pi B}{c}(\rho'-r(\varphi,y;\varphi',y')))d\varphi'dy' \end{aligned} \tag{5}$$

where $\lambda_c = c/f_c$ and B are the wavelength of the carrier frequency and the transmit bandwidth respectively, and the sinc function is defined as $sinc(x) = sin(x)/x$. Assuming that the size of the synthetic aperture along angular and $y-$directions are Φ and L_y respectively, the BPA imaging process based on the correlation can be conducted as

$$\begin{aligned} & I(\varphi',y') \\ &= \int_{-L_y/2+(\varphi-\varphi')v/\omega}^{L_y/2+(\varphi-\varphi')v/\omega}\int_{\varphi'-\Phi/2}^{\varphi'+\Phi/2} e_r(r(\varphi,y;\varphi',0) \\ &;\varphi,y+y')exp(j\frac{4\pi}{\lambda_c}r(\varphi,y;\varphi',0))d\varphi dy \end{aligned} \tag{6}$$

where $r(\varphi,y+y';\varphi',y') = r(\varphi,y;\varphi',0)$. Note that the integration interval with respect to y is affected by φ due to the nonorthogonality between the rotating and forward movement of radar.

C. Resolution Analysis

The use of the gradient is an effective tool to analyze the 2-D imaging resolution [22], [23]. In linear and rotation SAR systems, the transmit bandwidth and the 1-D movement can contribute two resolution vectors to the 2-D imaging resolution. With a combined 2-D movement, panoramic SAR can contribute three resolution vectors. In this subsection, the resolutions vectors of panoramic SAR are investigated compared with that of linear and rotation ones. Here, the unit vector along $x-$, $y-$ and $h-$directions are denoted as $\vec{i}$, $\vec{j}$, and $\vec{k}$ respectively.

Fig. 2a shows the synthetic aperture of linear SAR. With a fixed illumination perpendicular to the linear movement, two orthogonal resolution vectors provided by the transmit bandwidth and the linear synthetic aperture can be derived as

$$\vec{\delta_\rho} = \frac{c}{2B\cdot sin(\phi_h)}\cdot\vec{i} \tag{7}$$

and

$$\vec{\delta_L} = \frac{\lambda_c\sqrt{R_d^2+h_r^2}}{2L_y}\cdot\vec{j} \tag{8}$$

respectively, where R_d is the distance from the target to the center of the aperture in $xy-$plane and $\phi_h = arcsin(R_d/\sqrt{R_d^2+h_r^2})$ is the radar incident angle. Therefore, the imaging resolutions in $x-$ and $y-$directions, i.e., δ_x and δ_y, can be derived as $|\vec{\delta_\rho}|$ and $|\vec{\delta_L}|$ respectively, where $|.|$ denotes the module of the vector.

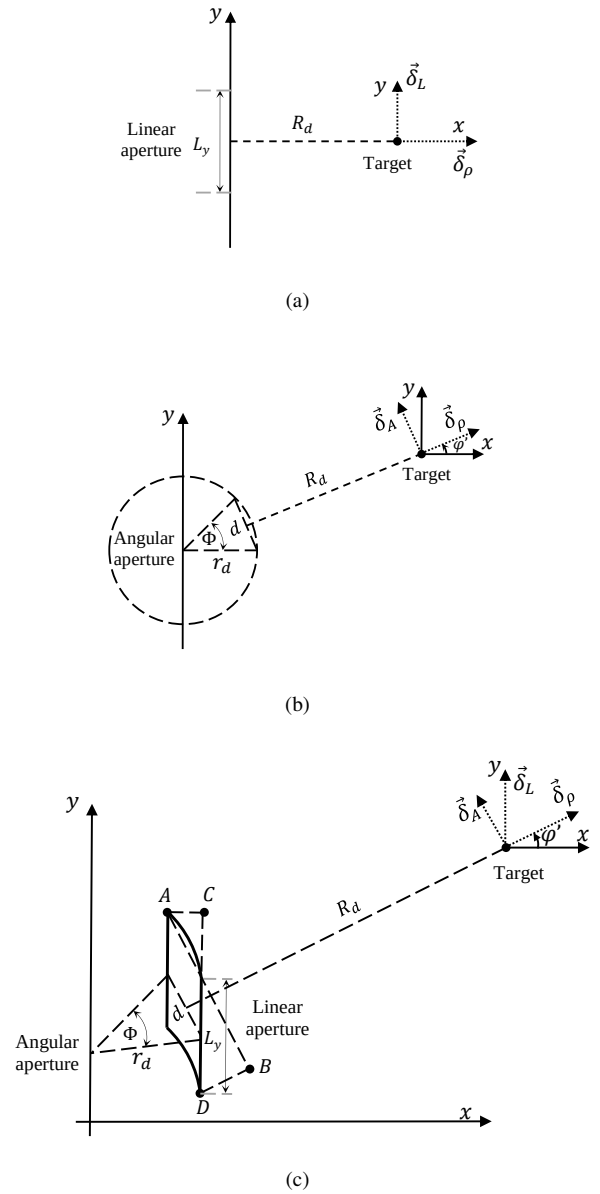

Fig. 2. Geometry of synthetic aperture in $xy-$plane: (a) linear SAR, (b) rotation SAR, and (c) panoramic SAR.

The synthetic aperture of rotation SAR is an arc with a radius of r_d and angle width of Φ as shown in Fig. 2b, and can be equivalent to a linear synthetic aperture with a length of d perpendicular to the radar range direction, thus providing two orthogonal resolution vectors as

$$\vec{\delta_\rho}(\varphi') = \frac{c}{2B\cdot sin(\phi_h)}\cdot(cos(\varphi')\vec{i}+sin(\varphi')\vec{j}) \tag{9}$$

and

$$\vec{\delta_A}(\varphi') = \frac{\lambda_c\sqrt{R_d^2+h_r^2}}{2d}\cdot(sin(\varphi')\vec{i}-cos(\varphi')\vec{j}) \tag{10}$$

respectively, where $d = 2r_d sin(\Phi/2)$ and φ' is the imaging angle of the radar in $xy-$plane. We can see that the δ_x and δ_y can be derived as the minimum values between $|\vec{\delta_\rho}(\varphi')|/|cos(\varphi')|$ and $|\vec{\delta_A}(\varphi')|/|sin(\varphi')|$, and between $|\vec{\delta_\rho}(\varphi')|/|sin(\varphi')|$ and $|\vec{\delta_A}(\varphi')|/|cos(\varphi')|$, respectively.

In panoramic SAR, the 2-D synthetic aperture can provide two nonorthogonal resolution vectors: one is similar to that provided by linear SAR, denoted as $\vec{\delta_L}$; the other one is similar to that provided by rotation SAR, denoted as $\vec{\delta_A}$. The range resolution vector $\vec{\delta_\rho}$ is always orthogonal to $\vec{\delta_A}$. Given an imaging target at φ', the geometry of the corresponding 2-D synthetic aperture is described in Fig. 2c. Obviously, the combined movement can formulate two equivalent linear synthetic apertures, i.e., the lengths of segments AB and CD corresponding to $\vec{\delta_A}$ and $\vec{\delta_L}$ respectively, which is valid due to $R_d \gg r_d$ in GB-SAR imaging scenarios. Note that these equivalent synthetic apertures are spatially variant with respect to φ' and larger than that of linear and rotation ones.

Similar to rotation SAR, the vector $\vec{\delta_\rho}$ and $\vec{\delta_A}$ can be easily derived as

$$\vec{\delta_\rho}(\varphi') = \frac{c}{2B \cdot sin(\phi_h)} \cdot (cos(\varphi')\vec{i} + sin(\varphi')\vec{j}) \tag{11}$$

and

$$\vec{\delta_A}(\varphi') = \frac{\lambda_c \sqrt{R_d^2 + h_r^2}}{2(d + L_y|cos(\varphi')|)} \cdot (sin(\varphi')\vec{i} - cos(\varphi')\vec{j}) \tag{12}$$

respectively, where the length of the segment AB is derived as $L_{AB} = d + L_y|cos(\varphi')|$. Due to the variant imaging angle φ', the linear synthetic aperture in panoramic SAR can be considered as a squint-forward-looking SAR imaging case. Based on the resolution vector provided by [23], $\vec{\delta_L}$ in panoramic SAR can be derived as

$$\vec{\delta_L}(\varphi') = \frac{\lambda_c \sqrt{R_d^2 + h_r^2}}{2(L_y + d|cos(\varphi')|)} \cdot \frac{1 + cot^2(\phi_h)}{\sqrt{cos^2(\varphi')sin^2(\varphi') + (cos^2(\varphi') + cot^2(\phi_h))^2}} \cdot \vec{u}(\varphi') \tag{13}$$

where the length of the segment CD is derived as $L_{CD} = d + L_y|cos(\varphi')|$, $cot(\phi_h) = cos(\phi_h)/sin(\phi_h)$ is the cotangent of ϕ_h, and $\vec{u}(\varphi')$ is the unit vector of $\vec{\delta_L}$, derived as

$$\begin{aligned} \vec{u}(\varphi') &= u_i(\varphi')\vec{i} + u_j(\varphi')\vec{j} \\ &= \frac{-cos(\varphi')sin(\varphi')}{\sqrt{cos^2(\varphi')sin^2(\varphi') + (cos^2(\varphi') + cot^2(\phi_h))^2}}\vec{i} \\ &+ \frac{cos^2(\varphi') + cot^2(\phi_h)}{\sqrt{cos^2(\varphi')sin^2(\varphi') + (cos^2(\varphi') + cot^2(\phi_h))^2}}\vec{j}. \end{aligned} \tag{14}$$

Similarly, the δ_x and δ_y can be derived as the minimum values among $|\vec{\delta_\rho}(\varphi')|/|cos(\varphi')|$, $|\vec{\delta_A}(\varphi')|/|sin(\varphi')|$ and $|\vec{\delta_L}(\varphi')|/|u_i(\varphi')|$), and among $|\vec{\delta_\rho}(\varphi')|/|sin(\varphi')|$, $|\vec{\delta_A}(\varphi')|/|cos(\varphi')|$ and $|\vec{\delta_L}(\varphi')|/|u_j(\varphi')|$), respectively.

We can see from (11) to (13) that a higher 2-D imaging resolution of panoramic SAR can be obtained due to more resolution vectors and larger equivalent synthetic apertures than that of linear and rotation ones.

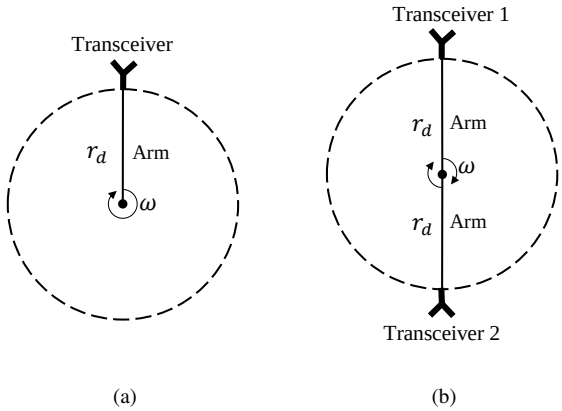

Fig. 3. Comparison between panoramic SAR modes: (a) single transceiver and (b) multiple transceivers.

D. Sampling Criteria

In a practical panoramic SAR, the data sampling must satisfy the Nyquist criterion, i.e., the phase shift from a corresponding spatial sample to the next must be less than π rad, to avoid the aliasing effects. Given the maximum wavenumber $k_{max} = 2\pi(f_c + B/2)/c$, the spatial sampling intervals with respect to φ and y from (4) are required by

$$\Delta\varphi \leq \frac{\pi\sqrt{r_d^2 + (R_d + L_y/2)^2 + h_r^2}}{2k_{max}(r_d R_d + L_y/2)} \tag{15}$$

and

$$\Delta y \leq \frac{\pi\sqrt{(r_d + R_d + L_y/2)^2 + h_r^2}}{2k_{max}(r_d + R_d + L_y/2)} \tag{16}$$

respectively. Similarly, the sampling interval $\Delta\tau$ of transmit FMCW signal from (3) is required by

$$\Delta\tau \leq \frac{c}{4K_r\sqrt{(r_d + R_d + L_y/2)^2 + h_r^2}}. \tag{17}$$

The derivations of (15), (16) and (17) are provided in Appendix A. From (1) and (2), $\Delta\varphi = \omega\Delta t$ and $\Delta y = v \cdot 2\pi/\omega$ are determined by the sampling interval with respect to t, angular and forward speeds ω and v. Therefore, the selection of these system parameters are limited by (15) and (16).

If a fast forward speed v is required, multiple transceivers, fixed on the tips of arms uniformly located around the rotating center as shown in Fig. 3b, can be adopted to increase the speed of the spatial sampling. Compared with the single-transceiver mode shown in Fig. 3a, the spatial sampling over one cycle can be achieved at the time cost of $2\pi/(N_r\omega)$ where N_r is the number of the transceivers. Therefore, the v can be increased N_r times given the same limited Δy. Note that the only difference between these two modes is the sampling speed which does not affect the BPA imaging process from (6).

III. Dynamic Piecewise Compensating Algorithm

The Fourier-based SAR imaging algorithms are no longer valid for panoramic SAR due to the nonlinear spatial sampling and the spatially variant 2-D synthetic aperture. Therefore, the

imaging process has to be conducted based on the correlation methods. However, the huge computational cost of the BPA from (6) is a great challenge limiting its application. In this section, we propose a novel fast DPC algorithm suitable for panoramic SAR imaging.

A. Imaging Principle

The BPA is always considered as the original imaging algorithm with a fully focusing capability. From (6), the difference between two arbitrary imaging results is actually the correlating with different slant range surface $r(\varphi, y; \varphi', y')$. To simplify the imaging process, the differences of the slant range surface between two adjacent imaging results, i.e., $D_\varphi(\varphi, y; \varphi', y') = r(\varphi, y; \varphi' + \Delta\varphi, y' + \Delta\varphi \cdot v/\omega) - r(\varphi, y; \varphi', y')$ and $D_y(\varphi, y; \varphi', y') = r(\varphi, y; \varphi', y' + \Delta y) - r(\varphi, y; \varphi', y')$, are investigated and some approximations are adopted to achieve a fast recursive imaging process from $I(\varphi', y')$ to $I(\varphi', y' + \Delta y)$ for panoramic SAR.

In panoramic SAR, the radius of the rotating beam center is far larger than that of the radar, i.e., $R_d \gg r_d$, thus deriving (2) as

$$\begin{aligned} &r(\varphi, y; \varphi', y') \\ &\approx \left(R_d^2 cos^2(\varphi') + r_d^2 + h_r^2 + (R_d sin(\varphi') + y' - y)^2\right)^{1/2} \\ &- \frac{r_d\left(R_d^2 cos^2(\varphi') + (R_d sin(\varphi') + y' - y)^2\right)^{1/2}}{\left(R_d^2 cos^2(\varphi') + r_d^2 + h_r^2 + (R_d sin(\varphi') + y' - y)^2\right)^{1/2}} \\ &\cdot cos(\varphi - \phi(\varphi')) \end{aligned} \tag{18}$$

where $\phi(\varphi') = arctan((R_d sin(\varphi') + y' - y)/(R_d cos(\varphi')))$. Therefore, the difference, $D_y(\varphi, y; \varphi', y')$, can be derived as

$$\begin{aligned} &D_y(y; \varphi', y') \\ &\approx \left(R_d^2 cos^2(\varphi') + r_d^2 + h_r^2 + (R_d sin(\varphi') + y' + \Delta y - y)^2\right)^{1/2} \\ &- \left(R_d^2 cos^2(\varphi') + r_d^2 + h_r^2 + (R_d sin(\varphi') + y' - y)^2\right)^{1/2} \end{aligned} \tag{19}$$

which is valid due to $R_d \gg L_y$.

To obtain $I(\varphi', y' + \Delta y)$ from $I(\varphi', y')$ recursively, the integration interval from (6) with respect to y can be firstly divided into P_y segments and (6) can be derived as

$$I(\varphi', y') \sum_{p_y=0}^{P_y-1} I_{p_y}(\varphi', y') \tag{20}$$

where

$$\begin{aligned} &I_{p_y}(\varphi', y') \\ &= \int_{y_{p_y}+(\varphi-\varphi')v/\omega}^{y_{p_y+1}+(\varphi-\varphi')v/\omega} \int_{\varphi'-\Phi/2}^{\varphi'+\Phi/2} e_r(r(\varphi, y; \varphi', 0); \varphi, y + y') \\ &\cdot exp(j\frac{4\pi}{\lambda_c} r(\varphi, y; \varphi', 0)) d\varphi dy \end{aligned} \tag{21}$$

where $y_{p_y} = -L_y/2 + p_y \cdot K_y \Delta y$, for $p_y = 0, 1, 2, ..., P_y - 1$, are the joint points of the segments over $[-L_y/2, L_y/2)$, K_y is the number of Δy over each segment, and $L_y = P_y \cdot K_y \cdot \Delta y$. Then, the difference $D_y(y; \varphi', 0)$ over p_yth segment can be approximated as a constant, expressed as

$$\widetilde{D}_y(p_y; \varphi') = \frac{1}{K_y} \sum_{k_y=0}^{K_y-1} D_y(y_{p_y} + k_y \Delta y; \varphi', 0) \tag{22}$$

which is the average value of $D_y(y; \varphi')$ with respect to y over $[y_{p_y}, y_{p_y+1})$. Finally, assuming that $e_r(r(\varphi, y; \varphi', y'), \varphi, y) \approx e_r(r(\varphi, y; \varphi', y' + \Delta y), \varphi, y)$, we have the recursive process

$$\begin{aligned} &I_{p_y}(\varphi', y' + \Delta y) \\ &\approx I_{p_y}(\varphi', y') exp(j\frac{4\pi}{\lambda_c} \widetilde{D}_y(p_y; \varphi')) \\ &- \int_{y_{p_y}-\Delta y+(\varphi-\varphi')v/\omega}^{y_{p_y}+(\varphi-\varphi')v/\omega} \int_{\varphi'-\Phi/2}^{\varphi'+\Phi/2} e_r(r(\varphi, y; \varphi', 0) \\ &; \varphi, y + y' + \Delta y) exp(j\frac{4\pi}{\lambda_c} r(\varphi, y; \varphi', 0)) d\varphi dy \\ &+ \int_{y_{p_y+1}-\Delta y+(\varphi-\varphi')v/\omega}^{y_{p_y+1}+(\varphi-\varphi')v/\omega} \int_{\varphi'-\Phi/2}^{\varphi'+\Phi/2} e_r(r(\varphi, y; \varphi', 0) \\ &; \varphi, y + y' + \Delta y) exp(j\frac{4\pi}{\lambda_c} r(\varphi, y; \varphi', 0)) d\varphi dy \end{aligned} \tag{23}$$

by which the difference of the slant range surface is firstly compensated and then the added and removed integrals are shifted in and out of the previous integral respectively.

We can see from (23) that added and removed integrals, defined as

$$\begin{aligned} &S_{p_y}(\varphi', y' + \Delta y) \\ &\approx \int_{y_{p_y}-\Delta y+(\varphi-\varphi')v/\omega}^{y_{p_y}+(\varphi-\varphi')v/\omega} \int_{\varphi'-\Phi/2}^{\varphi'+\Phi/2} e_r(r(\varphi, y; \varphi', 0) \\ &; \varphi, y + y' + \Delta y) exp(j\frac{4\pi}{\lambda_c} r(\varphi, y; \varphi', 0)) d\varphi dy \end{aligned} \tag{24}$$

must be obtained before calculating $I_{p_y}(\varphi', y' + \Delta y)$. To simplify the calculation of (24), a similar fast recursive process is proposed. Due to the impact of φ to the integration interval with respect to y seen in (6), $S_{p_y}(\varphi' + \Delta\varphi, y' + \Delta y + \Delta\varphi \cdot v/\omega)$ is obtained from $S_{p_y}(\varphi', y' + \Delta y)$ recursively. Firstly, $S_{p_y}(\varphi', y' + \Delta y)$ can be divided into P_φ segments and (24) can be derived as

$$S_{p_y}(\varphi', y' + \Delta y) = \sum_{p_\varphi=0}^{P_\varphi-1} S_{p_\varphi, p_y}(\varphi', y' + \Delta y) \tag{25}$$

where

$$\begin{aligned} &S_{p_\varphi, p_y}(\varphi', y' + \Delta y) \\ &= \int_{y_{p_y}-\Delta y+(\varphi-\varphi')v/\omega}^{y_{p_y}+(\varphi-\varphi')v/\omega} \int_{\varphi'+\varphi_{p_\varphi}}^{\varphi'+\varphi_{p_\varphi+1}} e_r(r(\varphi, y; \varphi', 0); \varphi \\ &, y + y' + \Delta y) exp(j\frac{4\pi}{\lambda_c} r(\varphi, y; \varphi', 0)) d\varphi dy \end{aligned} \tag{26}$$

where $\varphi_{p_\varphi} = -\Phi/2 + p_\varphi \cdot K_\varphi \Delta\varphi$, for $p_\varphi = 0, 1, 2, ..., P_\varphi - 1$, are the joint points of the segments over $[-\Phi/2, \Phi/2)$, K_φ is the number of $\Delta\varphi$ over each segment, and $\Phi = P_\varphi \cdot K_\varphi \cdot \Delta\varphi$.

Then, the corresponding $D_\varphi(\varphi, y; \varphi', 0)$ can be also approximated as a constant over p_φth segment, expressed as

$$\begin{aligned}&\widetilde{D}_\varphi(p_\varphi, p_y; \varphi')\\&= \frac{1}{K_\varphi}\sum_{k_\varphi=0}^{K_\varphi-1} D_\varphi(\varphi' + \varphi_{p_\varphi} + k_\varphi\Delta\varphi, y_{p_y} + (\varphi_{p_\varphi}\\&+ k_\varphi\Delta\varphi)\cdot v/\omega; \varphi', 0), \varphi \in [\varphi' + \varphi_{p_\varphi}, \varphi' + \varphi_{p_\varphi+1})\\&; y \in [y_{p_y} + \varphi_{p_\varphi}\cdot v/\omega, y_{p_y} + \varphi_{p_\varphi+1}\cdot v/\omega).\end{aligned} \tag{27}$$

Finally, assuming that $e_r(r(\varphi, y; \varphi', y'), \varphi, y) \approx e_r(r(\varphi, y; \varphi' + \Delta\varphi, y' + \Delta\varphi\cdot v/\omega), \varphi, y)$, we can have

$$\begin{aligned}&S_{p_y,p_\varphi}(\varphi' + \Delta\varphi, y' + \Delta y + \Delta\varphi\cdot v/\omega)\\&= S_{p_y,p_\varphi}(\varphi', y' + \Delta y)exp(j\frac{4\pi}{\lambda_c}\widetilde{D}_\varphi(p_\varphi, p_y; \varphi'))\\&- \int_{y_{p_y}-\Delta y+(\varphi-\varphi'-\Delta\varphi)v/\omega}^{y_{p_y}+(\varphi-\varphi'-\Delta\varphi)v/\omega}\int_{\varphi'+\varphi_{p_\varphi}}^{\varphi'+\Delta\varphi+\varphi_{p_\varphi}} e_r(r(\varphi, y; \varphi' + \Delta\varphi, 0)\\&; \varphi, y + y' + \Delta y + \Delta\varphi\cdot v/\omega)exp(j\frac{4\pi}{\lambda_c}r(\varphi, y; \varphi' + \Delta\varphi, 0))d\varphi dy\\&+ \int_{y_{p_y}-\Delta y+(\varphi-\varphi'-\Delta\varphi)v/\omega}^{y_{p_y}+(\varphi-\varphi'-\Delta\varphi)v/\omega}\int_{\varphi'+\varphi_{p_\varphi+1}}^{\varphi'+\Delta\varphi+\varphi_{p_\varphi+1}} e_r(r(\varphi, y; \varphi' + \Delta\varphi, 0)\\&; \varphi, y + y' + \Delta y + \Delta\varphi\cdot v/\omega)exp(j\frac{4\pi}{\lambda_c}r(\varphi, y; \varphi' + \Delta\varphi, 0))d\varphi dy.\end{aligned} \tag{28}$$

In summary, the recursive imaging process is achieved by segmenting the BPA integral and compensating the difference of the slant range surface dynamically based on the variant φ', thus named as dynamic piecewise compensating algorithm.

B. Imaging Implementation

The implementation of the fast DPC imaging in digital domain is presented in this subsection. Assuming that the $M = 2\pi/\Delta\varphi$ spatial samples are acquired over one rotation, the coordinate of the radar position $(\varphi, y) = (\omega t, vt)$ can be denoted as $(m\Delta\varphi, n\Delta y + m\Delta\varphi\cdot v/\omega)$, where m and n are the indexes describing the sampling time $t = (m + nM)\Delta t$. Given that the coordinate of the imaging pixel is equivalent to that of the radar, the recursive process shown in (28) can be derived as

$$\begin{aligned}&S_{p_y,p_\varphi}((m+1)\Delta\varphi, (n+1)\Delta y + (m+1)\Delta\varphi\cdot v/\omega)\\&= S_{p_y,p_\varphi}(m\Delta\varphi, (n+1)\Delta y + m\Delta\varphi\cdot v/\omega)exp(j\frac{4\pi}{\lambda_c}\widetilde{D}_\varphi(p_\varphi\\&, p_y; m\Delta\varphi))\\&- e_r(r((m+1)\Delta\varphi + \varphi_{p_\varphi}, y_{p_y} + \varphi_{p_\varphi}\cdot v/\omega; (m+1)\Delta\varphi, 0);\\&(m+1)\Delta\varphi + \varphi_{p_\varphi}, y_{p_y} + \varphi_{p_\varphi}\cdot v/\omega + (n+1)\Delta y + (m+1)\\&\cdot\Delta\varphi\cdot v/\omega)\cdot exp(j\frac{4\pi}{\lambda_c}r((m+1)\Delta\varphi + \varphi_{p_\varphi}, y_{p_y} + \varphi_{p_\varphi}\cdot v/\omega\\&; (m+1)\Delta\varphi, 0))\\&+ e_r(r((m+1)\Delta\varphi + \varphi_{p_\varphi+1}, y_{p_y} + \varphi_{p_\varphi+1}\cdot v/\omega; (m+1)\Delta\varphi\\&, 0); (m+1)\Delta\varphi + \varphi_{p_\varphi+1}, y_{p_y} + \varphi_{p_\varphi+1}\cdot v/\omega + (n+1)\Delta y\\&+ (m+1)\Delta\varphi\cdot v/\omega)\cdot exp(j\frac{4\pi}{\lambda_c}r((m+1)\Delta\varphi + \varphi_{p_\varphi+1}, y_{p_y}\\&+ \varphi_{p_\varphi+1}\cdot v/\omega; (m+1)\Delta\varphi, 0))\end{aligned} \tag{29}$$

Algorithm 1: DPC Imaging Algorithm

Initialization: Set $\mathbf{I}(p_y, m) = 0$ and $\mathbf{S}(p_y, p_\varphi, m) = 0$ for providing memory to $I_{p_y}(m\Delta\varphi, n\Delta y + m\Delta\varphi\cdot v/\omega)$ and $S_{p_y,p_\varphi}(m\Delta\varphi, n\Delta y + m\Delta\varphi\cdot v/\omega)$ respectively. Set $\mathbf{E}_r$ for storing the used compressed data. Given r_d and R_d, set $\mathbf{r}(p_y, p_\varphi, m) = r(m\Delta\varphi + \varphi_{p_\varphi+1}, y_{p_y} + \varphi_{p_\varphi+1}\cdot v/\omega; m\Delta\varphi, 0)$ calculated from (2), $\mathbf{D}_y(p_y, m) = \widetilde{D}_y(p_y; m\Delta\varphi)$ calculated from (22), and $\mathbf{D}_\varphi(p_y, p_\varphi, m) = \widetilde{D}_\varphi(p_\varphi, p_y; m\Delta\varphi)$ calculated from (27), respectively, for providing the required $\widetilde{D}_y(.)$, $\widetilde{D}_\varphi(.)$ and $r(.)$ to achieve the recursive processes, i.e., (29) and (30).

Recursive Imaging:

for *scanning time t*=Δt, $2\Delta t$,...,$(n\cdot M + m)\Delta t$,... **do**

(1) The received echoes $E_r(k, m\Delta\varphi, n\Delta y + m\Delta\varphi\cdot v/\omega)$ is firstly compressed by (5), and then storied into $\mathbf{E}_r$, meanwhile the unwanted compressed signal received previously is removed out of **DATA**;

(2) Based on $\mathbf{r}$, $\mathbf{D}_\varphi$ and the updated $\mathbf{E}_r$, $S_{p_y,p_\varphi}(m\Delta\varphi - \Phi/2, n\Delta y - L_y/2 + (m\Delta\varphi - \Phi/2)\cdot v/\omega)$ stored in $\mathbf{S}$ are updated recursively from (29).

(3) Based on $\mathbf{r}$, $\mathbf{D}_y$ and the updated $\mathbf{S}$, $S_{p_y}(m\Delta\varphi - \Phi/2, n\Delta y - L_y/2 + (m\Delta\varphi - \Phi/2)\cdot v/\omega)$ are firstly calculated from (25), and then substituted into (30) to update $I_{p_y}(m\Delta\varphi - \Phi/2, n\Delta y - L_y/2 + (m\Delta\varphi - \Phi/2)\cdot v/\omega)$ stored in $\mathbf{I}$. Finally, all of I_{p_y} are sumed up to obatin the imaging result at $(m\Delta\varphi - \Phi/2, n\Delta y - L_y/2 + (m\Delta\varphi - \Phi/2)\cdot v/\omega)$.

end

and $I_{p_y}(m\Delta\varphi, (n+1)\Delta y + m\Delta\varphi\cdot v/\omega)$ shown in (23) can be calculated as

$$\begin{aligned}&I_{p_y}(m\Delta\varphi, (n+1)\Delta y + m\Delta\varphi\cdot v/\omega)\\&= I_{p_y}(m\Delta\varphi, n\Delta y + m\Delta\varphi\cdot v/\omega)\cdot exp(j\frac{4\pi}{\lambda_c}\widetilde{D}_y(p_y; m\Delta\varphi))\\&- S_{p_y}(m\Delta\varphi, (n+1)\Delta y + m\Delta\varphi\cdot v/\omega)\\&+ S_{p_y+1}(m\Delta\varphi, (n+1)\Delta y + m\Delta\varphi\cdot v/\omega).\end{aligned} \tag{30}$$

Finally, the imaging result $I(m\Delta\varphi, (n+1)\Delta y + m\Delta\varphi\cdot v/\omega))$ is the sum of $I_{p_y}(m\Delta\varphi, (n+1)\Delta y + m\Delta\varphi\cdot v/\omega))$ based on (13).

The flow of the above-described process is summarized in **Algorithm 1**. Note that the correlation imaging can be achieved only after all the spatial samples over the 2-D synthetic aperture are acquired. Therefore, the target at $(m\Delta\varphi - \Phi/2, n\Delta y - L_y/2 + (m\Delta\varphi - \Phi/2)\cdot v/\omega)$ can be imaged only after the echo at $(n\cdot M + m)\Delta t$ is received.

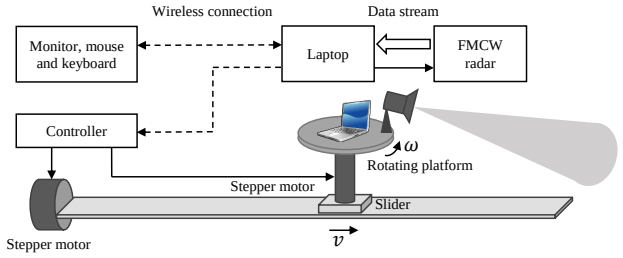

Fig. 4. Diagram of panoramic SAR prototype.

C. Complexity Analysis

To compare the complexity quantitatively, suppose that $N_y \times N_\varphi$ echoes can be acquired over the 2-D synthetic aperture and each echo consists of N_τ samples. For the sake of comparison, a $N_y \times N_\varphi$ image is reconstructed using BPA and DPC imaging algorithms respectively. In this subsection, we adopts the number of the required complex multiplications to describe the computational cost since the cost of implementing a complex addition is much lower than that of implementing a complex multiplication in practice.

Before the correlation imaging, $N_\tau log_2 N_\tau$ complex multiplications are required to process the range compression based on fast Fourier transform (FFT). After the range compression, the final imaging points are reconstructed independently using BPA from (6), by which each pixel imaging requires $N_y \times N_\varphi$ complex multiplications. By comparison, the DPC algorithm adopts a recursive imaging process. From (29) an (30), the update of a new imaging pixel requires $2P_yP_\varphi + 2P_y + 2P_\varphi + 1$ complex multiplications. Therefore, the total number of the complex multiplications required by the BPA and DPC algorithms are $N_yN_\varphi N_\tau log_2 N_\tau + N_y^2 N_\varphi^2$ and $N_yN_\varphi N_\tau log_2 N_\tau + N_yN_\varphi(2P_yP_\varphi + 2P_y + 2P_\varphi + 1)$ respectively. Since the P_y and P_φ are much smaller than N_y and N_φ, the proposed DPC algorithm can save much more computational cost than the BPA, which can be further demonstrated by the following experimental results.

IV. Panoramic SAR Prototype and Imaging Results

In this section, a panoramic SAR prototype is firstly built up based on a 77-GHz FMCW radar and a moving platform, and then the simulation and the experimental imaging results are presented respectively to validate the panoramic SAR principle and the DPC algorithm.

A. Panoramic SAR prototype

The deployment of the prototype based on the geometry of panoramic SAR is illustrated in Fig. 4. The rotating platform equipped with a FMCW radar is mounted on a slider, thus formulating the combined movement shown in Fig. 1c. This movement with simultaneous constant angular and forward speeds is achieved using two stepper motors with a controller, and the receiver frontend uses the AWR1843 single-chip 77-GHz FMCW radar sensor made by Texas Instruments [24].

TABLE I
Parameters of Panoramic SAR Prototype

Parameters	Values
Radius of rotating radar	$r_d = 0.06$ m
Radius of beam center	$R_d = 3$ m
Height of radar	$h_r = 0.5$ m
Angular and vertical speeds	$\omega = \pi/2$ rad/s and $v = 0.0025$ m/s
Time sampling interval of t	$dt = 4$ ms
Time sampling interval of τ	$d\tau = 0.4$ μs
Number of samples over a chirp	256
Carrier frequency and bandwidth	$f_c = 78.8$ GHz and B=3.6 GHz
Length of synthetic aperture	$L_y = 0.11$ m
Angle-width of synthetic aperture	$\Phi = 4\pi/25$ rad

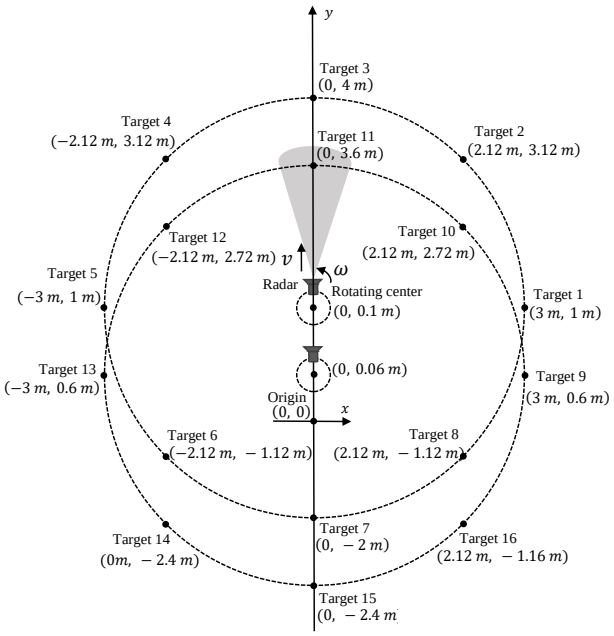

Fig. 5. Top view of point-target simulation scene.

For the ease of data capture, a laptop is directly placed on the center of the rotating platform. The laptop sends the command strings to the radar via micro universal serial bus (USB) ports, and the received raw data stream is transfered to the laptop via an Ethernet cable. Due to the rotating movement, the wireless connection between the laptop and the controller is adopted and the laptop is operated based on the wireless monitor, mouse and keyboard. The imaging processing and display are conducted by the laptop. Since the data sampling must satisfy the criteria discussed in Section II.D. the parameters of the panoramic SAR prototype are given in Table I.

B. Simulation Results

The point-target imaging performance of the panoramic SAR is investigated in this subsection. For the sake of comparison, the simulated raw data is generated based on the parameters of the prototype listed in Table I. Fig. 5 shows the top view of the simulation scene. Suppose that the rotating center moves along $y-$axis starting from the origin and the sixteen targets are located around the radar.

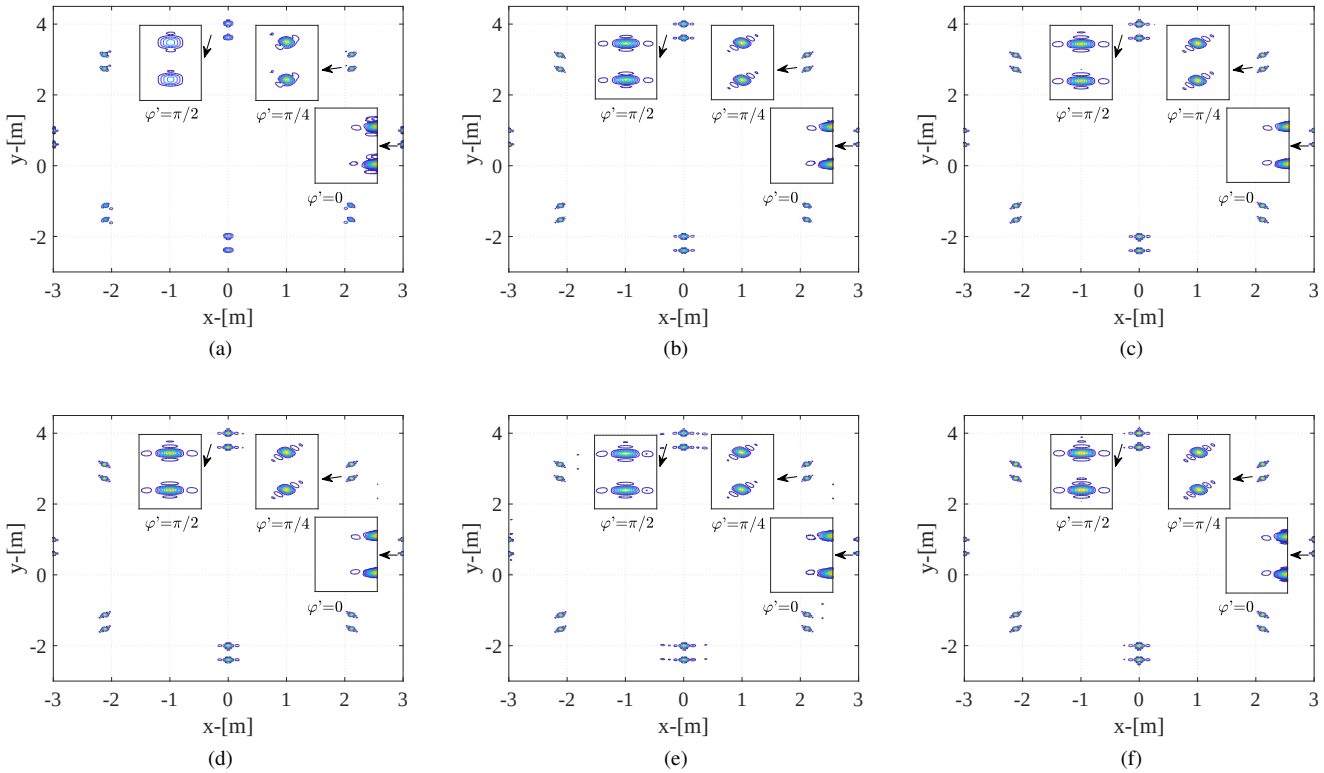

Fig. 6. Point-target images reconstructed by (a) DPC algorithm with $P_y = 2$ and $P_\varphi = 10$, (b) DPC algorithm with $P_y = 4$ and $P_\varphi = 10$, (c) DPC algorithm with $P_y = 6$ and $P_\varphi = 10$, (d) DPC algorithm with $P_y = 6$ and $P_\varphi = 8$, (e) DPC algorithm with $P_y = 6$ and $P_\varphi = 4$, and (f) BPA, respectively.

1) Imaging Resolution: Fig. 6f shows the image reconstructed by the BPA from (6). The imaging results of the targets from 1 to 16 correspond to $I(1,0)$, $I(1,\pi/4)$, ..., $I(1,3\pi/2)$, $I(1,7\pi/4)$, $I(0.6,0)$, $I(0.6,\pi/4)$, ..., $I(0.6,3\pi/2)$, and $I(0.6,7\pi/4)$, respectively. We can see that the imaging resolutions are independent of y' but vary with different φ'. Therefore, they are analyzed detailedly based on the different φ'. When $\varphi' = 0$ rad, the resolution vector $\vec{\delta_\rho}(0)$ is parallel to $x-$axis, $\vec{\delta_L}(0)$ and $\vec{\delta_A}(0)$ are parallel to $y-$axis, and the largest equivalent synthetic apertures, i.e., L_{AB} and L_{CD}, can be obtained. From (11) (12) and (13), the imaging resolutions at the targets 1 and 9 can be calculated as $\delta_x \approx 0.0422$ m and $\delta_y \approx 0.0353$ m, validated in Fig. 7a. As φ' is increased, $\vec{\delta_\rho}(\varphi')$ is always perpendicular to $\vec{\delta_A}(\varphi')$, but $\vec{\delta_\rho}(\varphi')$ and $\vec{\delta_L}(\varphi')$ become nonorthogonal and the equivalent synthetic apertures are shortened. Taking $\varphi' = \pi/4$ as an example, the imaging resolution at the target 2 and 10 can be calculated as $\delta_x = 0.0597$ m and $\delta_y = 0.0597$ m, validated in Fig. 7b. When φ' is increased to $\pi/2$, $\vec{\delta_A}(\pi/2)$ is parallel to $x-$axis, $\vec{\delta_L}(\pi/2)$ and $\vec{\delta_\rho}(\pi/2)$ are parallel to $y-$axis respectively, and the equivalent synthetic apertures become the shortest ones. Correspondingly, the imaging resolutions at the targets 3 and 11 can be calculated as $\delta_x = 0.1025$ m and $\delta_y = 0.0422$ m respectively, validated in Fig. 7c. Based on the variant φ', similar imaging resolutions can be obtained when $\varphi' = \varphi' + \pi$, which can be validated in Fig. 6e.

2) DPC imaging performance: The DPC imaging is proposed based on the approximated difference $\widetilde{D}_y(p_y;\varphi')$ and

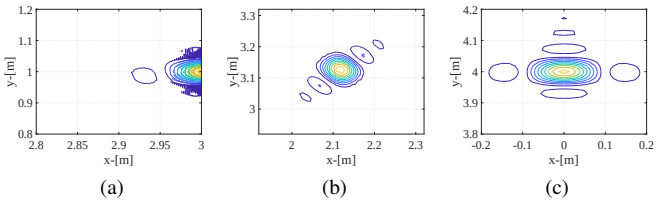

Fig. 7. BPA image from Fig. 6f enlarged at (a) Target 1, (b) Target 2, and (3) Target 3, respectively.

$\widetilde{D}_\varphi(p_\varphi,p_y;\varphi')$ between two adjacent imaging results. From (22) and (27), larger P_y and P_φ result in the more accurate approximations, thus obtaining better DPC imaging performance. From (29) and (30), $S_{p_y,p_\varphi}(\varphi',y')$ and $I_{p_y}(\varphi',y')$ are obtained recursively along rotating and forward directions, and thus the imaging abilities contributed by the rotating and linear movements are determined by P_φ and P_y respectively. Figs. 6a-6e show the images reconstructed by the DPC algorithm with different P_y and P_φ respectively. It is evident that the DPC algorithm performs better when P_y and P_φ are increased.

For more detailed analysis, the impact of P_y and P_φ to the imaging at different φ' is investigated. When $\varphi' = 0$, the imaging in $x-$axis is only determined by $\vec{\delta_\rho}(0)$ achieved by the range compression from (5) and thus independent of P_y and P_φ as seen in Figs. 6a-6f. The imaging in $y-$axis is determined by $\vec{\delta_L}(0)$ and $\vec{\delta_A}(0)$. Due to the equivalent synthetic apertures $L_{AB} = L_{CD} = d + L_y$ and $L_y > d$ under

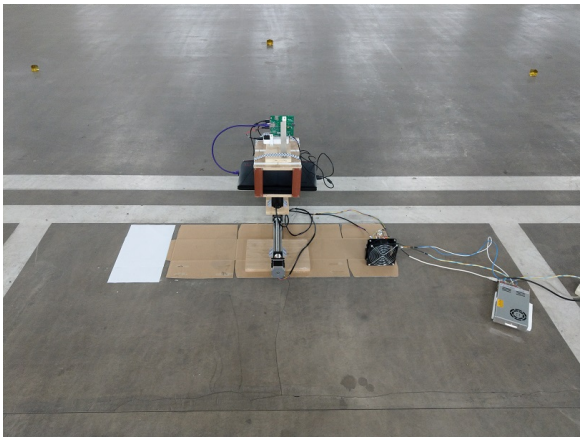

Fig. 8. Imaging scenario of Panoramic SAR prototype.

this prototype, the imaging ability contributed by the linear movement is more significant. The imaging results show that a worse imaging performance at $\varphi' = 0$ can be obtained when P_y is smaller. When φ' is increased, $\vec{\delta_\rho}(\varphi')$ and $\vec{\delta_L}(\varphi')$ become nonorthogonal and thus the imaging in $x-$ and $y-$axes are impacted by P_y and P_φ jointly. Take the imaging at $\varphi' = \pi/4$ as an example. $\vec{\delta_\rho}(\pi/4)$ is independent of P_y and P_φ. For $\vec{\delta_L}(\pi/4)$ and $\vec{\delta_A}(\pi/4)$, the corresponding equivalent synthetic apertures become $L_{AB} = d + L_y|cos(\pi/4)|$ and $L_{CD} = d|cos(\pi/4)| + L_y$ respectively. Due to $L_y \cdot cos(\pi/4) > d$ under this prototype, a worse imaging performance at $\varphi' = \pi/4$ can be obtained when P_y is smaller as seen in Figs. 6a. When φ' is increased to $\pi/2$, $\vec{\delta_L}(\pi/2)$ and $\vec{\delta_A}(\pi/2)$ are orthogonal, $L_{AB} = d$ and $L_{CD} = L_y$. Therefore, the imaging performance at $\varphi' = \pi/2$ in $x-$ and $y-$directions are determined by P_φ and P_y respectively which can be validated by the imaging results. Due to the nonorthogonal vectors $\vec{\delta_L}(\varphi')$ and $\vec{\delta_\rho}(\varphi')$, the approximation $e_r(r(\varphi, y; \varphi', y'), \varphi, y) \approx e_r(r(\varphi, y; \varphi', y' + \Delta y), \varphi, y)$ from (23) cannot be neglected in a high squint case. The error of this approximation deteriorates the imaging at $\varphi' = \pi/2$ in $y-$direction as seen in Fig. 6a and 6b. Therefore, a larger P_y is required to decrease the error.

In summary, the DPC imaging is actually determined by the three resolution vectors. $\vec{\delta_\rho}(\varphi')$ is only determined by the range compression, and $\vec{\delta_L}(\varphi')$ and $\vec{\delta_\rho}(\varphi')$ correspond to the equivalent synthetic apertures $L_{AB} = d + L_y|cos(\varphi')|$ and $L_{CD} = d|cos(\varphi')| + L_y$ respectively. Therefore, the impacts of P_y and P_φ to the imaging performance of $\vec{\delta_L}(\varphi')$ and $\vec{\delta_\rho}(\varphi')$ vary with the φ'.

C. Experimental Results

In this subsection, the experiment based on the prototype is implemented. Fig. 8 presents the imaging scenario. Since the similar imaging resolutions can be obtained when imaging at φ' and $\varphi' + \pi$ as seen from Fig. 6f, we place three metal targets randomly in front of the panoramic SAR prototype, whose imaging results can validate the proposed panoramic SAR. After setting up the parameters, the radar scanning based on the combined movement is triggered when the laptop sends the command strings to the radar and controller respectively.

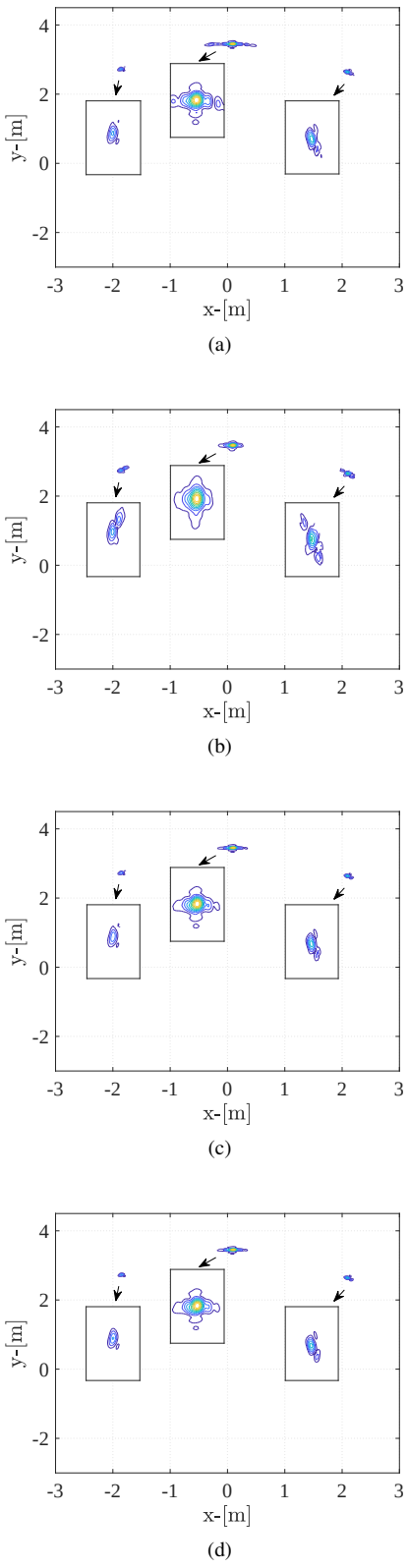

Fig. 9. Real images reconstructed by (a) DPC algorithm with $P_y = 6$ and $P_\varphi = 4$, (b) DPC algorithm with $P_y = 2$ and $P_\varphi = 10$, (c) DPC algorithm with $P_y = 6$ and $P_\varphi = 10$, and (d) BPA, respectively.

After the data acquisition, the proposed imaging process in digital domain is performed in the laptop with a 2.8-GHz CPU by using Matlab 2019.

TABLE II
TIME COST COMPARISON

Algorithms	Time(second)
DPC with $P_y = 2$ and $P_\varphi = 10$	6.993
DPC with $P_y = 6$ and $P_\varphi = 4$	9.169
DPC with $P_y = 6$ and $P_\varphi = 10$	15.058
BPA from (6)	79.618

Fig. 9 shows the image reconstructed by the BPA and the DPC algorithm with different P_y and P_φ respectively, in which the three targets with the different radar cross section (RCS) can be observed clearly. The imaging results can further validate the analysis of the imaging resolutions and performance in Section II.C and Section IV.B. We can see that the imaging resolutions are spatially variant with different φ' and the DPC imaging performs better with increased P_y and P_φ. When $P_y = 6$ and $P_\varphi = 10$, a similar imaging result can be obtained, compared with that of the BPA.

To demonstrate the efficiency of the DPC algorithm, the time cost comparison is shown in Table II. It is evident that time cost of the proposed algorithm is much lower than that of the BPA. Note that there is a tradeoff between the imaging performance and the computational cost as larger P_y and P_φ complicate the implementation of the proposed imaging process. Therefore, to design a practical panoramic SAR system, P_y and P_φ should be selected properly based on the simulated point-target imaging results.

V. CONCLUSION

We have developed a panoramic SAR which is a combination of linear and rotation GB-SARs, thus offering many advantages. A larger panoramic observed scene can be provided and a 2-D synthetic aperture is formulated to improve the imaging resolutions. This paper fully investigates the principle of panoramic SAR, including system geometry, BPA, resolutions analysis, and sampling criteria. A novel DPC algorithm is further proposed to reduce the complexity significantly. The prototype of panoramic SAR is built up, and the corresponding simulation and experimental results are provided to validate the proposed panoramic SAR principle and the DPC algorithm.

The work presented in this paper establishes a solid theoretical foundation of panoramic SAR concept. On this basis, more new GB-SAR applications can be designed to suit different imaging scenarios.

APPENDIX A
DERIVATION OF SAMPLING CRITERIA

Based on the Nyquist criterion, the upper bounds of the sampling intervals, $\Delta\varphi$, Δy, and $\Delta\tau$ are derived as

$$2k_{max}(r(\varphi+\Delta\varphi,y;\varphi',y')-r(\varphi,y;\varphi',y'))\le 2k_{max} \cdot (r(\varphi+\Delta\varphi,y+\Delta\varphi\cdot v/\omega;\varphi',y')-r(\varphi,y;\varphi',y'))\le\pi \tag{31}$$

$$2k_{max}(r(\varphi,y+\Delta y;\varphi',y')-r(\varphi,y;\varphi',y'))\le\pi \tag{32}$$

and

$$2\Delta k r(\varphi,y_r;\varphi',y_r')\le\pi. \tag{33}$$

The difference in wavenumber is $\Delta k = 2\pi(f_c + K_r(\tau+\Delta\tau))/c - 2\pi(f_c+K_r(\tau))/c = 2\pi K_r\Delta\tau/c$. The differences $r(\varphi+\Delta\varphi,y;\varphi',y')-r(\varphi,y;\varphi',y')$ and $r(\varphi,y+\Delta y;\varphi',y')-r(\varphi,y;\varphi',y')$ can be derived as $r'(\varphi,y;\varphi',y')|_\varphi\cdot\Delta\varphi$ and $r'(\varphi,y;\varphi',y')|_y\cdot\Delta y$ respectively, where $f'(x,y)|_x$ denotes the first derivative of $f(x,y)$ with respect to x. Therefore, we can have

$$\Delta\varphi\le\frac{\pi r(\varphi,y;\varphi',y')}{2k_{max}|R_d r_d sin(\varphi-\varphi')+(y-y')cos(\varphi)|}, \tag{34}$$

$$\Delta y\le\frac{\pi r(\varphi,y;\varphi',y')}{2k_{max}|r_d sin\varphi - R_d sin\varphi' + y - y'|} \tag{35}$$

and

$$\Delta\tau\le\frac{c}{4K_r r(\varphi,y;\varphi',y')} \tag{36}$$

where $\Delta\varphi$, Δy and $\Delta\tau$ must be smaller than the minimum values of the right side, thus obtaining (15), (16) and (17) respectively.

REFERENCES

[1] A. Moreira, P. Prats-Iraola, M. Younis, G. Krieger, I. Hajnsek, and K. P. Papathanassiou, "A Tutorial on Synthetic Aperture Radar," *IEEE Geoscience and Remote Sensing Magazine*, vol. 1, no. 1, pp. 6–43, 2013.

[2] J. H. Gonzalez, M. Bachmann, R. Scheiber, and G. Krieger, "Definition of ICESat Selection Criteria for Their Use as Height References for TanDEM-X," *IEEE Transactions on Geoscience and Remote Sensing*, vol. 48, no. 6, pp. 2750–2757, June 2010.

[3] X. M. Li, S. Lehner, and T. Bruns, "Ocean Wave Integral Parameter Measurements Using Envisat ASAR Wave Mode Data," *IEEE Transactions on Geoscience and Remote Sensing*, vol. 49, no. 1, pp. 155–174, Jan 2011.

[4] C.-C. Liu, S.-J. Chang, G.-Y. Huang, and Y.-Z. Lin, "A 10-bit 50-MS/s SAR ADC with A Monotonic Capacitor Switching Procedure," *IEEE Journal of Solid-State Circuits*, vol. 45, no. 4, pp. 731–740, 2010.

[5] G. Nico, D. Leva, G. Antonello, and D. Tarchi, "Ground-Based SAR Interferometry for Terrain Mapping: Theory and Sensitivity Analysis," *IEEE Transactions on Geoscience and Remote Sensing*, vol. 42, no. 6, pp. 1344–1350, 2004.

[6] D. Leva, G. Nico, D. Tarchi, J. Fortuny-Guasch, and A. Sieber, "Temporal Analysis of A Landslide by Means of a Ground-Based SAR Interferometer," *IEEE Transactions on Geoscience and Remote Sensing*, vol. 41, no. 4, pp. 745–752, 2003.

[7] "Landslide Monitoring by Ground-Based Radar Interferometry: A Field Test in Valdarno (Italy)," *International Journal of Remote Sensing*, vol. 24, no. 6, pp. 1385–1391, 2003.

[8] G. Antonello, N. Casagli, P. Farina, D. Leva, G. Nico, A. J. Sieber, and D. Tarchi, "Ground-Based SAR Interferometry for Monitoring Mass Movements," *Landslides*, vol. 1, no. 1, pp. 21–28, 2004.

[9] M. Pieraccini, "Real Beam vs. Synthetic Aperture Radar for Slope Monitoring," 2013, pp. 1627–1630.

[10] H. Lee, S. J. Cho, N. H. Sung, and J. H. Kim, "Development A GB-SAR (I): System Configuration and Interferometry," *KOREAN JOURNAL OF REMOTE SENSING*, vol. 23, no. 4, pp. 237–245, 2007.

[11] H. Klausing and W. Keydel, "Feasibility of A Synthetic Aperture Radar with Rotating Antennas (ROSAR)," in *IEEE International Conference on Radar*, 1990, pp. 51–56.

[12] D. Li, H. Liu, Y. Liao, and X. Gui, "A Novel Helicopter-Borne Rotating SAR Imaging Model and Algorithm Based on Inverse Chirp-Z Transform Using Frequency-Modulated Continuous Wave," *IEEE Geoscience and Remote Sensing Letters*, vol. 12, no. 8, pp. 1625–1629, 2015.

[13] S. Gishkori, L. Daniel, M. Gashinova, and B. Mulgrew, "Imaging for A Forward Scanning Automotive Synthetic Aperture Radar," *IEEE Transactions on Aerospace and Electronic Systems*, vol. 55, no. 3, pp. 1420–1434, 2019.

[14] D. Jasteh, E. G. Hoare, M. Cherniakov, and M. Gashinova, "Experimental Low-Terahertz Radar Image Analysis for Automotive Terrain Sensing," *IEEE Geoscience and Remote Sensing Letters*, vol. 13, no. 4, pp. 490–494, 2016.

[15] H. Lee, J.-H. Lee, K.-E. Kim, N.-H. Sung, and S.-J. Cho, "Development of A Truck-Mounted Arc-Scanning Synthetic Aperture Radar," *IEEE Transactions on Geoscience and Remote Sensing*, vol. 52, no. 5, pp. 2773–2779, 2014.
[16] M. Pieraccini and L. Miccinesi, "Arcsar: Theory, Simulations, and Experimental Verification," *IEEE Transactions on Microwave Theory and Techniques*, vol. 65, no. 1, pp. 293–301, 2017.
[17] Y. Luo, H. Song, R. Wang, Y. Deng, F. Zhao, and Z. Xu, "Arc FMCW SAR and Applications in Ground Monitoring," *IEEE Transactions on Geoscience and Remote Sensing*, vol. 52, no. 9, pp. 5989–5998, 2014.
[18] A. Ishimaru, T.-K. Chan, and Y. Kuga, "An Imaging Technique Using Confocal Circular Synthetic Aperture Radar," *IEEE Transactions on Geoscience and Remote Sensing*, vol. 36, no. 5, pp. 1524–1530, 1998.
[19] K. Hu, X. Zhang, S. He, H. Zhao, and J. Shi, "A Less-Memory and High-Efficiency Autofocus Back Projection Algorithm for SAR Imaging," *IEEE Geoscience and Remote Sensing Letters*, vol. 12, no. 4, pp. 890–894, 2015.
[20] L. Ulander, H. Hellsten, and G. Stenstrom, "Synthetic Aperture Radar Processing Using Fast Factorized Back Projection," *IEEE Transactions on Aerospace and Electronic Systems*, vol. 39, no. 3, pp. 760–776, 2003.
[21] L. Zhang, H.-l. Li, Z.-j. Qiao, M.-d. Xing, and Z. Bao, "Integrating Autofocus Techniques with Fast Factorized Back-Projection for High-Resolution Spotlight SAR Imaging," *IEEE Geoscience and Remote Sensing Letters*, vol. 10, no. 6, pp. 1394–1398, 2013.
[22] G. Cardillo, "On the Use of the Gradient to Determine Bistatic SAR Resolution," in *International Symposium on Antennas and Propagation Society, Merging Technologies for the 90's*, 1990, pp. 1032–1035 vol.2.
[23] R. Hu, B. S. M. R. Rao, A. Murtada, M. Alaee-Kerahroodi, and B. Ottersten, "Automotive Squint-Forward-Looking SAR: High Resolution and Early Warning," *IEEE Journal of Selected Topics in Signal Processing*, vol. 15, no. 4, pp. 904–912, 2021.
[24] T. Instruments, "AWR1843 Single-Chip 77- and 79-GHz FMCW Radar Sensor," http://www.ti.com/lit/ds/swrs222/swrs222.pdf, Dec 2018, original document from Texas Instruments.